Flow-Through Drying of Porous Media

Jagannathan Mahadevan
Dept. of Petroleum Engineering, University of Tulsa, Tulsa, OK 74104

Mukul M. Sharma
Dept. of Chemical and Petroleum Engineering, The University of Texas at Austin, Austin, TX 78712

Yannis C. Yortsos
Dept. of Chemical Engineering, University of Southern California, Los Angeles, CA 90089

DOI 10.1002/aic.10859
Published online April 26, 2006 in Wiley InterScience (www.interscience.wiley.com).

The flow of a gas (saturated or dry) through a porous medium, which is partially occupied by a liquid phase, causes evaporation. The latter occurs, even if the inlet gas is fully saturated, as a result of volume expansion. This process, referred to as flow-through drying, is important in a variety of natural and industrial applications, such as convective drying, fuel cells, and natural gas production, which is the context of this work. In this article, a mathematical model is developed to understand the process and to predict drying rates and the evolution of liquid saturation profiles. The model includes the effects of gas compressibility and capillarity. Compressibility effects account for the evaporation into the saturated gas phase, whereas the capillary pressure gradients cause the liquid flow that leads to spreading of the saturation profile. Two important parameters, a normalized viscous pressure drop across the medium and capillary "wicking" number, control the two respective regimes. Capillary-driven flow from regions of high saturation to regions of low saturation leads to more uniform saturation profiles or spreading drying fronts. The results are compared against experimental data obtained by X-ray imaging. © 2006 American Institute of Chemical Engineers *AIChE J,* 52: 2367–2380, 2006

Introduction

The removal of trapped wetting liquids from porous media is important in applications such as the drying of paper, wood, or construction materials, in catalysts, fuel cells, and others. In the context of the recovery of gas from subsurface reservoirs, condensed liquids that block the pore space—and thus hinder gas production—must also be removed. Typically, this is accomplished by the physical displacement of the wetting phase by a nonwetting phase, in a drainage process. Viscous forces exerted by the injected phase cause the displacement of a part of the wetting phase from the porous medium. Drainage is very common in a number of applications in subsurface hydrology or in oil recovery. However, at its conclusion, typically after several pore volumes of injection, a substantial fraction of the wetting liquid is either immobilized or remains trapped in the pore space, and effectively stops flowing. Removing this trapped liquid is a nontrivial task. When the wetting liquid is sufficiently volatile, it can be removed by drying.

The drying of porous media has been studied by several investigators.[1-7] The majority of the studies have focused on diffusion-driven drying: an unsaturated gas phase flows over the external surface of a porous medium occupied by the wetting liquid, which evaporates into the unsaturated gas. As long as the liquid is in direct contact with the flowing gas, drying is controlled by external mass transfer. However, when the liquid recedes deeper into the porous medium, and hydraulic continuity (either through liquid menisci or through films) is

Correspondence concerning this article should be addressed to J. Mahadevan at jmahadevan@utulsa.edu.

lost, drying becomes controlled by the much slower rate of gas diffusion.

A different but related problem is *flow-through drying*, in which evaporation occurs into a gas phase injected into the porous medium. As early as 1949, Allerton et al.[8] studied flow-through drying in packed beds of crushed quartz or other materials, where the injected gas phase was dry. An evaporation regime sets in, after the immiscible displacement of the initial liquid by the injected gas. More recently, laboratory experiments[9,10] reported results in flow-through drying for the removal of "water blocks" from gas-producing wells in a subsurface porous medium. In these, the injected gas phase was fully saturated (wet-gas), with the drying, after the displacement, occurring as a result of gas expansion. The evaporation regime was shown to last for a large number of pore volumes of gas injected (order thousand). Higher pressure drops, hydrophobicity of the pore surface, and solvent addition were shown[9] to improve the efficiency during evaporation. Zuluaga and Lake[11] presented a mathematical model for flow-through drying using fractional flow theory, in the absence of compressibility effects, and under conditions of dry-gas injection. They focused on the traveling evaporation front that separates two regions, an upstream state of dry gas without any liquid from a downstream state of fully saturated gas and trapped liquid. Traveling evaporation fronts, in a geothermal context under nonisothermal conditions, were also investigated by Woods and Fitzgerald.[12]

The objective of this work is to provide a mathematical model of flow-through drying applicable to both wet- and dry-gas injection, after the end of the viscous displacement regime, when the liquid is trapped and does not flow. For this, gas compressibility and capillary effects must be included. Gas compressibility is necessary for evaporation into the saturated gas. Capillarity is needed to model the spreading of the liquid saturation profile across drying fronts and is of particular importance when the bulk liquid does not flow, as is the case considered here.

For drying of porous media, both phenomenological and pore network models have been used in the past. In the context of diffusion-driven drying (dry gas flowing over an exposed porous medium) Luikov,[7] Whitaker,[13] and others developed a drying theory based on volume-averaging methods, assuming a constant gas pressure. In parallel, efforts have been undertaken using pore-network models,[4] intended to provide information either ignored or lumped into average properties in volume-averaging. The pore-network studies correctly describe drying as a form of drainage (thus as a percolation process), controlled by the diffusion of the evaporating gas to the external surface. Early studies neglected the important liquid counterflow through macroscopic films along pore walls.[14-17] However, Laurindo and Prat[18] showed that experimental drying rates differed significantly from those calculated numerically from pore-network models, when film flow was not included. More recently, Yiotis et al.[19] presented a pore-network model that included corner films, to account for such counterflows, in conjunction with a percolation model. They showed that, depending on the capillary properties of the process, the presence of macroscopic films can dramatically affect the drying rates. Capillary pressure–driven film flow (the capillary-wicking effect) enhances drying by transporting liquid from the deeper recesses of the porous medium to the regions nearer to the surface, where drying rates can be greater: the stronger the capillarity of the porous medium, the larger the enhancement in drying. This effect is incorporated in the analysis presented below.

In contrast to diffusion-driven drying, flow-through drying is much less understood. It is one of the objectives of this work to make progress in this direction, by developing a model that includes the two controlling mechanisms mentioned above: gas compressibility and capillarity. The model will be based on continuum concepts under the assumption of local (pore-scale) thermodynamic equilibrium. We account for capillary effects in the evaporation regime by including liquid flow through macroscopic films[19] in corners of pores. The sensitivity of the results to various parameters—particularly to the viscous pressure drop in the gas phase and the capillarity of the porous medium, under the two different conditions of wet-gas and dry-gas injection—is investigated. The model prediction is compared against experimental results for saturation profiles in flow-through drying, obtained by linear X-ray attenuation.

The article is organized as follows: First, we develop the general conservation equations for gas and water. The resulting governing equation contains a reaction-like sink term that captures evaporation as a result of gas compressibility. We then consider the solution of the problem for the two cases of wet-gas and dry-gas injection, respectively. Simple solutions, when capillary effects are strong, will be provided for both cases. In wet-gas injection, these describe the smoothing out of saturation profiles over time arising from capillary pressure–driven flows (wicking). In dry-gas injection, they describe the motion of the traveling drying front, which arises as a result of gas concentration gradients. Sensitivity analysis and a comparison with experimental data obtained by X-ray attenuation are provided to validate the model.

Mathematical Model

We consider the simultaneous, two-phase flow of two immiscible fluids, a single-component liquid (denoted by subscript w), and a binary gas phase (denoted by subscript g). Under one-dimensional (1D) flow conditions, the conservation equations for the water and gas components are as follows:

$$\phi\rho_w \frac{\partial S_w}{\partial t} + \phi \frac{\partial}{\partial t}\left(\rho_g S_g \frac{M_w y_w}{M_g}\right) + \rho_w \frac{\partial u_w}{\partial x} + \frac{\partial}{\partial x}\left(\rho_g \frac{M_w y_w}{M_g} u_g\right) = 0 \quad (1)$$

$$\phi \frac{\partial}{\partial t}\left(\rho_g S_g \frac{M_w(1-y_w)}{M_g}\right) + \frac{\partial}{\partial x}\left[\rho_g \frac{M_w(1-y_w)}{M_g} u_g\right] = 0 \quad (2)$$

where S denotes saturation (volumetric fraction of the pore space), ϕ is porosity, ρ is mass density, M is the molecular weight, y denotes mole fraction in the gas phase, and u_g is the gas-phase velocity. Under the two assumptions that the system is isothermal and the gas phase is ideal we can rewrite the above in the form

$$\frac{\partial}{\partial t}\left[\beta S_w + \alpha(1 - S_w)\right] + \frac{1}{\phi}\frac{\partial}{\partial x}\left(\beta f_w u_T + \alpha f_g u_T\right) = 0 \quad (3)$$

$$\phi\frac{\partial}{\partial t}\left[(1 - y_w) P_g S_g\right] + \frac{\partial}{\partial x}\left[(1 - y_w) P_g f'_g u_T\right] = 0 \quad (4)$$

where we introduced the concentrations $\alpha = y_w P_g/R_g T$ and $\beta = \rho_w/M_w$, in the gas and liquid phases, respectively, and expressed the fluid-phase velocities as a fraction of the total velocity: $u_w = f'_w u_T$, $u_g = f'_g u_T$, where subscript T stands for the total flow rate. Note that $\beta \gg \alpha$. The fractional flow terms can be obtained from a standard application of Darcy's law for multiphase flow.[20] For the liquid phase we have,

$$f'_w = f_w\left(1 + \frac{kk_{rg}}{u_T\mu_g}\frac{\partial P_c}{\partial x} - \frac{kk_{rg}\Delta\rho_g}{u_T\mu_g}\right) \quad (5)$$

where

$$f_w = \frac{\dfrac{kk_{rw}}{\mu_w}}{\dfrac{kk_{rw}}{\mu_w} + \dfrac{kk_{rg}}{\mu_g}} \quad (6)$$

The corresponding expression for the gas phase follows from the identity $f'_w + f'_g = 1$.

In Eqs. 5 and 6, k denotes permeability; $k_{rj}(S_w)$ is the relative permeability of phase j, a function of the liquid saturation; μ denotes viscosity; $P_c(S_w)$ is the capillary pressure function; $\Delta\rho$ is the difference in density; and g is the acceleration of gravity in the direction of displacement (which here will coincide with the downward vertical direction). The three terms on the right-hand side (RHS) of Eq. 5 denote flow driven by viscous pressure gradient (first term), capillarity (second term), and buoyancy (third term). In our application, viscous forces dominate during the displacement regime, capillary forces will be more important during the evaporation regime, whereas gravitational forces are negligible (see below). Equations 3–6, along with constitutive expressions for the relative permeabilities and the capillary pressure, and using Raoult's law for phase equilibrium, provide a complete description of the problem. We have assumed ideal solution and ideal gas, necessary for Raoult's law to hold true:

$$y_w(x, t) = \frac{P_s}{P_g} \qquad \text{if } S_w(x, t) > 0 \quad (7)$$

As we previously noted, the initial part of flow-through drying consists of the immiscible displacement of the liquid by the injected gas. This regime lasts over several pore volumes (of the order 100 or so), after which the liquid saturation reaches an almost steady-state profile and the bulk liquid ceases to flow. During this period, evaporation is negligible and the problem can be solved by the standard equations for immiscible flow in porous media.[20] For simplicity, these will not be repeated below. After the end of immiscible displacement, evaporation is the main mechanism of water removal. This is the regime of primary interest in this article and is explored in detail below.

The total flow velocity

To analyze the evaporation regime, we first note that because gas mobility dominates, Eq. 4 can be rewritten as

$$\frac{\phi\alpha}{(\beta - \alpha)}\frac{\partial}{\partial t}\left(\Pi S_g\right) + \frac{\partial}{\partial x}\left(\Pi u_T\right) = 0 \quad (8)$$

where we have defined $\Pi = P_g - P_s(T)$. This can be further simplified by introducing the "drying" time coordinate $\tau = t\alpha/(\beta - \alpha)$, in terms of which we find

$$\varepsilon\frac{\partial}{\partial\tau}\left[\Pi(1 - S_w)\right] + \frac{1}{\phi}\frac{\partial}{\partial x}\left(\Pi u_T\right) = 0 \quad (9)$$

where we defined

$$\varepsilon = \frac{\alpha}{\beta - \alpha} \quad (10)$$

Given that $\beta \gg \alpha$, we have $\varepsilon \ll 1$. Thus, in the drying timescale (τ), to leading order, Eq. 9 becomes

$$\frac{\partial}{\partial x}\left[\Pi u_T\right] = 0 \quad (11)$$

Equation 11 states that in the evaporation regime and outside of a boundary layer in time (that is, the viscous displacement regime), the mass flow rate of the gas phase is practically independent of the axial coordinate. This result reflects the slowness of evaporation, when the flowing gas is almost fully saturated. By noting that the total flow velocity essentially consists of the gas phase, $u_T = -\lambda_{rg}(S_w)(\partial\Pi/\partial x)$, where we defined the gas mobility $\lambda_{rg} = kk_{rg}(S_w)/\mu_g$, neglected any liquid mobility, and taken the vapor pressure independent of the axial location, Eq. 11 can be integrated to yield

$$\Pi_0^2 - \Pi^2 = 2A(\tau)\int_0^x \frac{1}{\lambda_{rg}(S_w)}\,dx \quad (12)$$

where the constant $A(\tau)$ is evaluated at the outlet end of the sample (at location L),

$$A(\tau) = \frac{\Pi_0^2 - \Pi_L^2}{2\displaystyle\int_0^L \frac{1}{\lambda_{rg}(S_w)}\,dx} \quad (13)$$

and where subscripts 0 and L denote inlet and outlet, respectively. Thus, we finally find an explicit expression for the total flow velocity,

$$u_T = \frac{A(\tau)}{\Pi} = \frac{A(\tau)}{\sqrt{\Pi_o^2 - 2A(\tau)\int_0^x \frac{dx}{\lambda_{rg}(S_w)}}} \tag{14}$$

The governing equation for liquid evaporation

Consider, next, Eq. 3 under the conditions of the evaporation regime. We first note that the gravity term is negligible compared to capillarity (in the experiments to be reported below, the Bond number $k\Delta\rho g/\gamma$, expressing the importance of gravity over capillarity, was of the order of 10^{-8}). Further, at the end of viscous displacement, the relative mobility of the liquid is negligible compared to that of the gas. Using these two assumptions, we may then rewrite Eq. 3 in the new time coordinate as follows:

$$\frac{\partial S_w}{\partial \tau} + \frac{1}{\phi}\frac{\partial u_T}{\partial x} + \frac{1}{\varepsilon}\frac{1}{\phi}\frac{\partial}{\partial x}\left(f_w \frac{kk_{rg}}{\mu_g}\frac{\partial P_c}{\partial x}\right) = 0 \tag{15}$$

The second term on the left-hand side (LHS) above represents compressibility-driven drying: It is nonzero only if the gas phase is compressible (compare with Eq. 11). Using Eq. 14 for the gas velocity, then we write Eq. 15 as

$$\frac{\partial S_w}{\partial \tau} + \frac{A(\tau)}{\phi}\frac{\partial}{\partial x}\left(\frac{1}{\sqrt{\Pi_o^2 - 2A(\tau)\int_0^x \frac{dx}{\lambda_{rg}}}}\right) + \frac{1}{\varepsilon}\frac{1}{\phi}\frac{\partial}{\partial x}\left(f_w \frac{kk_{rg}}{\mu_g}\frac{\partial P_c}{\partial x}\right) = 0 \tag{16}$$

The physical meaning of Eq. 16 is better understood if we make the simplification that the relative gas mobility is constant with distance (an assumption that is most likely to be obeyed in the later part of the drying process). Then, the integral term simplifies and Eq. 16 becomes

$$\frac{\partial S_w}{\partial \tau} + \frac{1}{\varepsilon}\frac{1}{\phi}\frac{\partial}{\partial x}\left(f_w \frac{kk_{rg}}{\mu_g}\frac{dP_c}{dS_w}\frac{\partial S_w}{\partial x}\right) + \frac{\lambda_{rg}}{4}\frac{1}{\phi}\sqrt{\frac{(\Pi_0^2 - \Pi_L^2)}{L}}\left(\frac{\Pi_0^2 L}{\Pi_0^2 - \Pi_L^2} - x\right)^{-3/2} = 0 \tag{17}$$

Equation 17 is essentially a diffusion–reaction equation, where compressibility-driven drying acts as the reaction (sink) term and capillarity acts as diffusion. The sink rate increases with the gas mobility, the flow rate, and the distance from the injection end, reflecting factors that favor gas expansion. We also express the capillary diffusivity term as

$$-f_w \frac{kk_{rg}}{\mu_g}\frac{dP_c}{dS_w} \approx -\frac{kk_{rw}}{\mu_w}\frac{dP_c}{dS_w} = \frac{a_{gm}\gamma r_c}{\mu_w} D(S_w) \tag{18}$$

where γ is the interfacial tension, r_c is the mean pore throat size ($r_c = \sqrt{8k/\phi}$, from bundle of capillary tubes model), and a_{gm} is a geometric constant (see below). Although we will comment on expressions for the capillary diffusivity in a later section, we note in advance that tighter porous media, higher interfacial tensions, and lower flow rates all increase the capillary diffusivity.

Equation 17 can be written in dimensionless form by introducing the dimensionless variables $x_D = x/L$ and $t_D = \tau/\tau^*$, where $\tau^* = 4\phi\mu_g\Pi_0^3 L^2/k(\Pi_0^2 - \Pi_L^2)^2$; the dimensionless pressure drop $C = (\Pi_0^2 - \Pi_L^2)/\Pi_0^2$; and a dimensionless number $N_{Wi} = 4a_{gm}\gamma r_c \Pi_0^3 \mu_g/\varepsilon\mu_w(\Pi_0^2 - \Pi_L^2)^2 k$, which we term as the "wicking number." Parameter C denotes the effect of pressure drop on compressibility-driven drying. The wicking number denotes the ratio between capillary and viscous forces and it is essentially the inverse of a modified capillary number. In the above notation, Eq. 17 becomes

$$\frac{\partial S_w}{\partial t_D} = N_{Wi}\frac{\partial}{\partial x_D}\left[D(S_w)\frac{\partial S_w}{\partial x_D}\right] - \frac{1}{\left[\int_0^1 \frac{d\xi}{k_{rg}(S_w)}\right]^2 k_{rg}(S_w)}\left[1 - C\frac{\int_0^{x_D}\frac{d\xi}{k_{rg}(S_w)}}{\int_0^1 \frac{d\xi}{k_{rg}(S_w)}}\right]^{-3/2} \tag{19}$$

which is an expanded version of the form

$$\frac{\partial S_w}{\partial t_D} = N_{Wi}\frac{\partial}{\partial x_D}\left[D(S_w)\frac{\partial S_w}{\partial x_D}\right] - \frac{\partial u_D}{\partial x_D} \tag{19a}$$

where we defined the dimensionless velocity

$$u_D = \frac{2}{C\left[\int_0^1 \frac{d\xi}{k_{rg}(S_w)}\right]}\left[1 - C\frac{\int_0^{x_D}\frac{d\xi}{k_{rg}(S_w)}}{\int_0^1 \frac{d\xi}{k_{rg}(S_w)}}\right]^{-1/2} \tag{19b}$$

The latter will be found useful in various parts of the sections that follow. Again, we note that in the limit of spatially constant gas mobility, Eq. 19 takes the simpler form

$$\frac{\partial S_w}{\partial t_D} = N_{Wi}\frac{\partial}{\partial x_D}\left[D(S_w)\frac{\partial S_w}{\partial x_D}\right] - k_{rg}(1 - Cx_D)^{-3/2} \tag{20}$$

which shows a reaction term that increases with the distance from the injection end solely because of compressibility. The geometric factor and the interfacial tension serve to increase the wicking number, which in turns make the diffusive term in Eq. 20 larger. On the other hand, the pressure drop, permeability, and the drying scale factor all serve to decrease the wicking number, thus to decrease the effect of the diffusive term. It is interesting to note that the pressure drop appears both in the source term and in the diffusive term. It acts to strengthen the source term while weakening the diffusive term. Equation 19 will be solved based on an assumed initial condition for the

saturation profile (from the end of the displacement period), and the outlet boundary condition,

$$D(S_w)\left.\frac{\partial S_w}{\partial x_D}\right|_1 = 0 \tag{21}$$

which imposes the no-flux boundary condition for the wetting phase at the outlet. The inlet boundary condition will depend on whether the injected gas is wet or dry. These two different cases will be described separately below.

The constitutive relations

Included in the governing Eq. 19 are two constitutive relations—the relative permeability to gas and the capillary diffusivity—both of which depend on the wetting phase saturation. A number of expressions, such as the Brooks and Corey[21] or the van Genuchten[22] equations, exist in the literature. Percolation and effective medium theories can be used to provide justification for such expressions. During the displacement period,[23] power laws of the Corey form are typically assumed for the relative permeabilities

$$k_{rg} = k_{rg}^0(1 - \overline{S_w})^{n_g} \qquad \text{if } S_w > S_{wr} \tag{22a}$$

$$k_{rg} = 1 - (1 - k_{rg}^0)\frac{\langle S_w\rangle}{S_{wr}} \qquad \text{if } S_w \le S_{wr} \tag{22b}$$

$$k_{rw} = k_{rw}^0 \overline{S_w}^{n_w} \tag{22c}$$

where k_{rg} and k_{rg}^0 are prefactors, n_g and n_w are positive exponents, and $\overline{S_w} = (S_w - S_{wr})/(1 - S_{wr} - S_{gr})$ is the reduced saturation. For the capillary pressure curve, the following two-parameter expression attributed to van Genuchten, is used here:

$$P_c = \frac{1}{\alpha'}\left((\overline{S_w})^{-(1/m)} - 1\right)^{1/n} \tag{23}$$

where

$$m = 1 - \frac{1}{n} \qquad \text{and} \qquad \alpha' \sim \frac{1}{\gamma}\sqrt{\frac{k}{\phi}}$$

During the evaporation regime, wetting flow is driven by capillarity in the form of macroscopic films along the pore walls. Several authors[16,24,25] studied film flow along the corners of long smooth capillaries with polygonal cross sections. Assuming Poiseulle-type law,[24,25] Yiotis et al.[19] expressed the volume flow rate Q_x in a single long film of radius of curvature r as

$$Q_x = -\frac{a_g r^4}{\mu_l}\frac{\partial P_w}{\partial x} \tag{24}$$

where a_g is a dimensionless geometric factor. The volume fraction (saturation) of the liquid across the capillary is approximately

$$S_w = b\frac{r^2}{r_c^2} \tag{25}$$

where b is another geometric constant of order one. Thus, the relative permeability of the wetting phase can be obtained from the following expressions:

$$\frac{i\phi a_g r^4}{c r_c^2} = \frac{i\phi a_g r_c^2}{cb^2} S_w^2 = d r_c^2 k_{rw} \tag{26}$$

where we assumed a total of i films in a capillary, the cross-sectional area of the capillary was taken to be cr_c^2, and the fully occupied flow conductivity of the capillary was assumed equal to dr_c^2, as expected from Poiseuille's law. The various geometric constants reflect the pore geometry and will be left unspecified, in the absence of more information. One may then obtain the simple result

$$k_{rw} = BS_w^2 \tag{27}$$

where in the dimensionless parameter $B = i\phi a_g/cdb^2$, we combined all the unknown geometric constants. It is to be noted that this scaling is similar to the well-known relationships such as the Corey model. The capillary pressure across the film is

$$P_c = P_g - P_w = \frac{\gamma}{r} \tag{28}$$

which upon substitution from Eq. 25 and differentiation gives

$$\frac{dP_c}{dS_w} = -\frac{\gamma b^{1/2}}{2r_c} S_w^{-3/2} \tag{29}$$

By substituting Eqs. 27 and 29 into Eq. 18, we can now identify the capillary diffusivity dependency as

$$\left(\frac{kBb^{1/2}}{2r_c^2}\right)\frac{\gamma r_c}{\mu_w} S_w^{1/2} = a_{gm}\frac{\gamma r_c}{\mu_w} D(S_w) \tag{30}$$

where

$$D(S_w) = S_w^{1/2} \tag{30a}$$

and the geometric constant is given by

$$a_{gm} = \frac{kBb^{1/2}}{2r_c^2} \tag{30b}$$

The expression for the gas relative permeability is still approximated by Eqs. 22a and 22b. Equations 22 and 29 provide the constitutive relations during the evaporation regime. We note that the capillary diffusivity vanishes when the liquid saturation vanishes, suggesting hypodiffusion.[26] This is based on the postulate of macroscopic (corner) film flow. As the saturation decreases to very low values, however, this

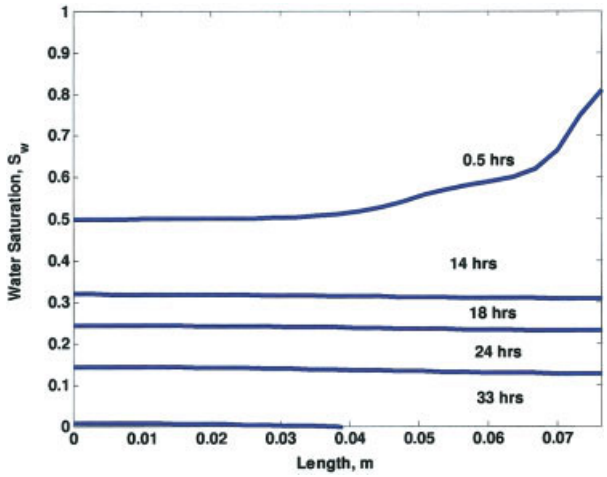

Figure 1. Numerical water saturation profiles for flow-through drying and the injection of wet gas at different times after the end of the displacement regime.

Gas flow is from left to right. The flow parameters are from Table 1 (B-15a) with the value of the capillary "wicking" number equal to 123. [Color figure can be viewed in the online issue, which is available at www.interscience.wiley.com]

postulate may not necessarily hold because thin films of the van der Waals type will develop and control the flow, giving rise to the opposite behavior, that is, an increasing diffusivity as the saturation decreases. This process, known as *hyperdiffusion*, has been explored in some detail in previous studies.[26] Because it is associated with very low saturations, where many of the other assumptions we made above may also lose validity, however, this regime will be neglected in this study.

Results

The governing Eq. 19 was solved under two different injection conditions: fully saturated (wet-gas) and dry gas. Because of important differences in their behavior, the two cases will be discussed separately.

Injection of wet gas

Injection of wet gas highlights the importance of compressibility-driven evaporation. This process also arises naturally in gas production from a gas reservoir, when large pressure gradients near the production well cause evaporation of water. Because the injected gas is fully saturated, the inlet boundary condition is one of zero flux for the liquid; thus, in addition to Eq. 21, we also have

$$D(S_w)\left.\frac{\partial S_w}{\partial x_D}\right|_0 = 0 \tag{31}$$

The solution of Eq. 19 subject to the boundary conditions in Eqs. 21 and 31 was computed numerically using finite differences and with the integral of the relative permeability in Eq. 19 calculated explicitly. The evolution of the saturation profile for two different values of the capillary "wicking" number is shown in Figures 1 and 2, respectively. The data from Table 1, B-15, were used with the initial condition obtained from the end of the displacement process.[27] In both cases, the profiles decrease uniformly, which results from the liquid redistribution within the porous medium through the mechanism of capillarity noted above, captured here through the diffusive term in Eq. 19. Capillarity is fundamental to the establishment of a uniform profile. Figure 1 shows that after a small initial transient, the profiles become flat. This is in contrast to Figure 2, which corresponds to negligible capillarity, $N_{Wi} = 0$. Because of the acceleration of drying at the outlet end, and the absence of capillarity, the profiles in Figure 2 show a significant decrease with distance. A comparison of the two figures shows that capillarity significantly accelerates the drying process.

The flat saturation profiles resulting from strong capillary conditions can be derived analytically by integrating Eq. 19 or its equivalent expression (Eq. 19a) and substituting Eq. 19b to yield

$$\frac{1}{k_{rg}(\langle S_w\rangle)}\frac{d\langle S_w\rangle}{dt_D} = -\frac{2}{C}[(1-C)^{-1/2}-1] \tag{32}$$

where brackets indicate an average across the sample. The term on the RHS in the above is the difference in the gas velocity at the exit and at the entrance, showing explicitly the effect of compressibility-driven evaporation. Equation 32 can be readily integrated. For instance, if we adopt the model Eq. 22b for the relative permeability, we obtain the explicit result

$$\ln\left[1-\frac{(1-k_{rg}^0)}{S_{wr}}\langle S_w\rangle\right] = \ln\left[1-\frac{(1-k_{rg}^0)}{S_{wr}}\langle S_w|_{t_D=0}\rangle\right] + \frac{(1-k_{rg}^0)}{S_{wr}}\frac{2}{C}[(1-C)^{-1/2}-1]t_D \tag{33}$$

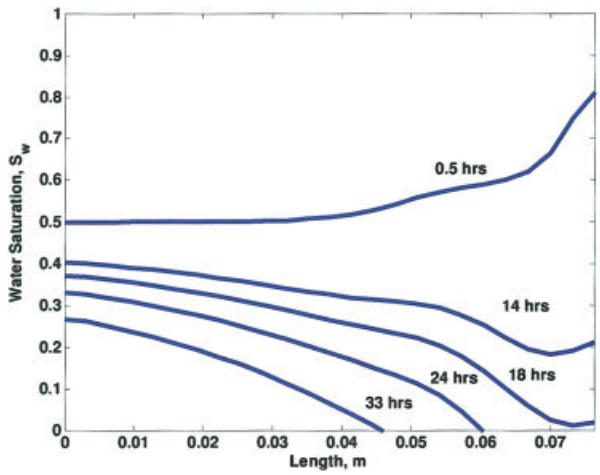

Figure 2. Numerical water saturation profiles for flow-through drying and the injection of wet gas at different times after the end of the displacement regime.

Gas flow is from left to right. The flow parameters are from Table 1 (B-15a) with the capillary effects suppressed (the value of capillary "wicking" number is equal to zero). [Color figure can be viewed in the online issue, which is available at www.interscience.wiley.com]

Table 1. Flow Properties of Berea and Tight-Gas Samples Used

Type	Permeability* k (mD)	Porosity* ϕ	Modified Geometric Constant** a_{gm}	Gas Relative Permeability Parameters*,†	
				k_{rgo}	n_g
Berea (B-15a)	85	0.17	0.002	0.65	2.4
Tight gas (TG)	0.01	0.066	0.002	0.25	2
Berea (B-15b)	76	0.16	0.00005	0.3	2.0

* The flow properties for the rock samples are obtained directly from experiments.
**The modified geometric constant, for both Berea samples, is determined from the best fit of saturation profiles with the model solution.
† Straight-line relative permeabilities used for saturations less than $S_{wr} = 0.5$, residual gas saturation, $S_{gr} = 0.0$. Length of porous sample, $L = 0.076$ m.

which can also be rewritten as

$$\langle S_w \rangle = \frac{\exp\left\{\dfrac{(1-k_{rg}^0)}{S_{wr}}\dfrac{2}{C}\left[(1-C)^{-1/2}-1\right]t_D\right\}S_{wr}}{(1-k_{rg}^0)} \qquad (34)$$

The evolution of the average saturation in time is plotted in Figure 3, for the same conditions as in Figures 1 and 2. The variation follows the expression in Eq. 34 rather well. The effect of the capillary "wicking" number becomes important at later stages and is shown to speed up drying, compared to the case with no capillary-induced flow ($N_{Wi} = 0$). In the latter, when drying is completed at the downstream section, where drying rates are higher, there is no mechanism to transport liquid to the dry region; thus, evaporation of the liquid proceeds slowly. This is not so in the capillary case, where through capillary action, liquid is redistributed to the drier downstream region, where drying is faster, thus resulting into a faster overall drying. In Figure 3, the exponent corresponding to the exponential in Eq. 34 is small and thus the variation of the saturation is almost linear. Figure 4 shows similar results, but for a low permeability porous medium for the conditions specified in Table 1. In the tighter porous medium, the effect of capillarity becomes important early and accelerates drying by a faster rate.

Equation 34 shows that drying terminates at the dimensionless time

$$t_D^* = \frac{\ln\left[1-\dfrac{(1-k_{rg}^0)}{S_{wr}}\langle S_w|_{t_D=0}\rangle\right]}{\dfrac{(1-k_{rg}^0)}{S_{wr}}\dfrac{2}{C}\left[1-(1-C)^{-1/2}\right]} \qquad (35)$$

the dimensional counterpart of which is

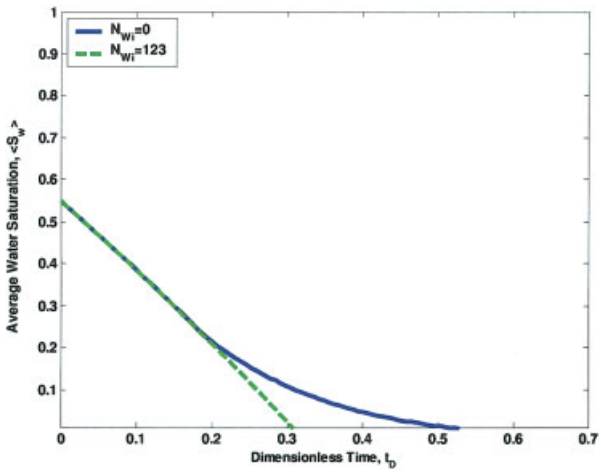

Figure 3. Effect of capillarity on the evolution of the average saturation in flow-through drying and the injection of wet gas, as a function of the dimensionless time.

A higher capillary "wicking" number captures stronger film flow effects, compared to the zero capillary "wicking" number that corresponds to no film flow. Drying is faster at a higher capillary "wicking" number, causing a more rapid decrease in the saturations. The flow parameters are from Table 1 (B-15a). [Color figure can be viewed in the online issue, which is available at www.interscience.wiley.com]

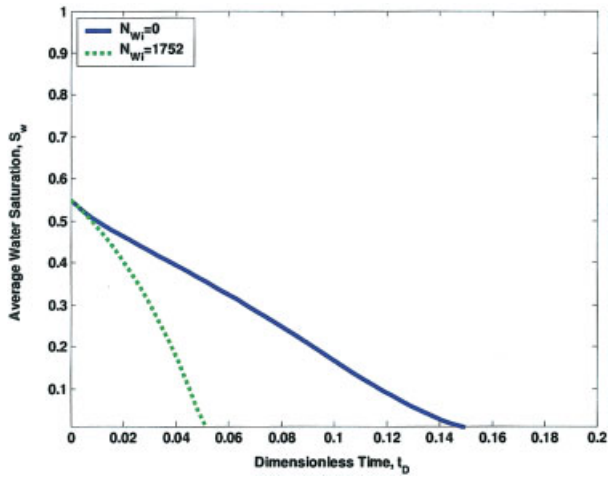

Figure 4. Effect of capillarity on the evolution of the average saturation in flow-through drying and the injection of wet gas, as a function of the dimensionless time.

A higher capillary "wicking" number captures stronger film flow effects, compared to the zero capillary "wicking" number that corresponds to no film flow. Drying is faster at a higher capillary "wicking" number, causing a more rapid decrease in the saturations. The flow parameters are from Table 1 (TG) for a pressure drop of 10 atm. [Color figure can be viewed in the online issue, which is available at www.interscience.wiley.com]

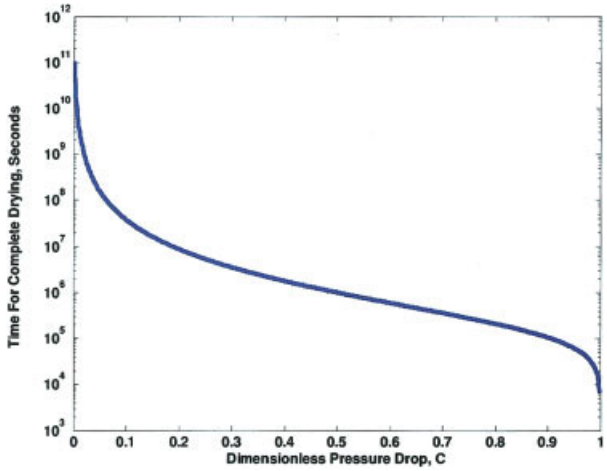

Figure 5. Plot of the dimensional time for the complete drying of a core in flow-through drying and injection of wet gas as a function of the dimensionless pressure drop.

The flow parameters are from Table 1 (B-15a). The time for complete drying asymptotically approaches infinity as the dimensionless pressure drop goes to zero. [Color figure can be viewed in the online issue, which is available at www.interscience.wiley.com]

$$t^* = \frac{2\phi\mu_g L^2 RT\rho_w S_{wr}}{(1-k_{rg}^0)kC[1-(1-C)^{-1/2}][P_{g0}-P_s(T)]P_{g0}y_w M_w} \times \ln\left[1-\frac{(1-k_{rg}^0)}{S_{wr}}\langle S_w|_{t_D=0}\rangle\right] \quad (36)$$

The variation of t^* as a function of the dimensionless pressure drop variable, C, is plotted in Figure 5. As expected, the time decreases as C increases, and when C approaches zero, where gas expansion is negligible, it becomes infinitely large. Equation 36 also shows that the time to complete drying increases with increasing gas viscosity and the length of the sample, and decreases with higher permeability, higher flow rates, and a more volatile species.

A different way of showing these results is by plotting the evolution of the overall relative permeability of the gas, which because of its dependency on the liquid saturation will also evolve in time as drying proceeds. This is particularly useful for practical applications in gas reservoirs, where the gas flow rate will depend on the amount of liquid saturation in the pore space. The evolution of the gas flow from one that is partially blocked by liquid to a fully dry condition depends on the rate of evaporation, which in turn is coupled to the rate of gas flow, as previously shown. Figure 6 shows results for the evolution of the gas flow rate (the overall gas relative permeability) from a partially saturated porous medium corresponding to the conditions of Figure 4 and for two cases, where capillarity is either included or neglected, respectively. Consistent with Figure 4, the plot shows that in the presence of capillarity, the recovery of gas flow rate is much faster. Again, this is attributed to capillary transport of liquid from low drying-rate regions to high drying-rate regions. This reduces the liquid saturation and leads to a greater gas relative permeability.

A comparison of the numerical results with wet-gas injection experiments will be shown in a later section.

Dry-gas injection

When the injected gas is dry, there are two qualitative differences from the saturated case: First, the inlet boundary condition is different because the dry inlet favors evaporation and capillarity transports liquid in a countercurrent fashion. Because there is no net influx of water vapor, the inlet boundary condition is, in dimensional variables,

$$-u_w|_{x=0} = \frac{\alpha}{\beta}u_g|_{x=0} \qquad \text{if } S_w|_{x=0} > 0 \quad (37)$$

and

$$S_w|_{x=0} = 0 \quad (38)$$

otherwise. Equation 38 expresses the fact that the liquid transported by capillary action through film flow is instantly partitioned in the gas phase and returns downstream to the porous medium. Using the previously derived expressions we can rewrite the boundary condition as

$$-\frac{kk_{rw}}{\mu_w}\frac{\partial P_c}{\partial x}\bigg|_0 = \frac{\alpha}{\beta}u_g|_{x=0} \quad (39)$$

and in dimensionless notation

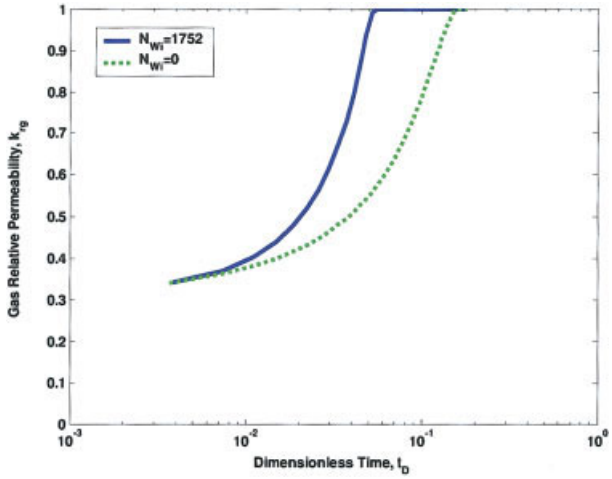

Figure 6. Effect of capillarity on the evolution of the overall permeability of gas in flow-through drying and injection of wet gas, as a function of the dimensionless time.

A higher capillary "wicking" number captures stronger film flow effects, compared to the zero capillary "wicking" number that corresponds to no film flow. Drying is faster at a higher capillary "wicking" number, causing a more rapid increase in the gas permeability. The flow parameters are from Table 1 (TG) for a pressure drop of 10 atm. [Color figure can be viewed in the online issue, which is available at www.interscience.wiley.com]

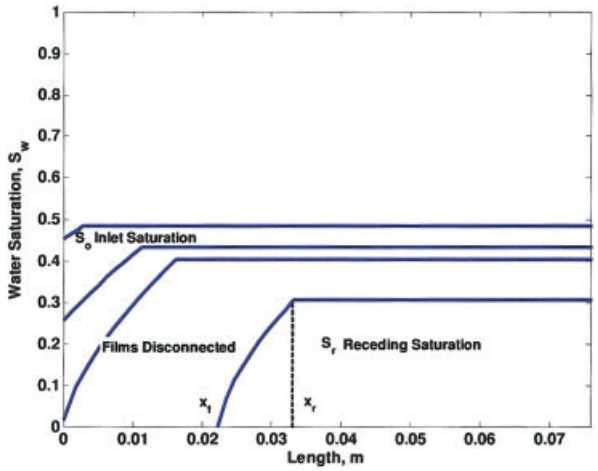

Figure 7. Schematic of the saturation profile during injection of a dry gas into a porous medium and after the displacement regime has been completed.

In the initial stage [denoted as stage (a) in the text] the films are connected to the inlet. At a later stage [denoted as stage (b) in the text], films disconnect and a moving drying front propagates into the porous medium. The receding saturation decreases as a result of evaporation by gas expansion. [Color figure can be viewed in the online issue, which is available at www.interscience.wiley.com]

$$N_{Wi}CD(S_w)\left.\frac{\partial S_w}{\partial x_D}\right|_0 = \frac{2}{\int_0^1 \frac{d\xi}{k_{rg}(S_w)}} \tag{40}$$

The second difference is the appearance of a dry region near the inlet, which will propagate downstream (see schematic of Figure 7), in a manner to be determined. Ahead of the moving front, evaporation proceeds as in the wet-gas case, at the rates dictated by gas expansion.

Figure 8 shows results for saturation profiles using the parameters of Table 1, B-15b, corresponding to experiments[27] in a sandstone core. The simulations in this figure are for the case where capillarity is not negligible. The features of the saturation profile include: a time-decreasing flat profile ahead of the drying front; an inlet saturation that decreases in time; the disconnection of the films (zero liquid saturation) at the inlet; and the onset of a moving front, with the two boundaries x_r and x_f moving in time. Figure 10 (see below) shows results corresponding to a much smaller capillary "wicking" number. We note that sharp fronts traveling almost at constant velocity. Comparison with the experiments will be provided below.

To analyze the profiles shown in Figures 8 and 9, we will consider two different stages: (a) when the inlet saturation is nonzero, where the liquid is connected to the inlet through liquid films; and (b) when it is zero, indicating that a dry region has developed within the porous medium. We assume conditions of strong capillarity, where the downstream saturation profile is flat and decreases with time because of compressibility-driven evaporation. The variable saturation upstream, where drying is attributed to the injected dry gas (as shown in the schematic of Figure 7), will be approximated using a quasi-steady assumption.

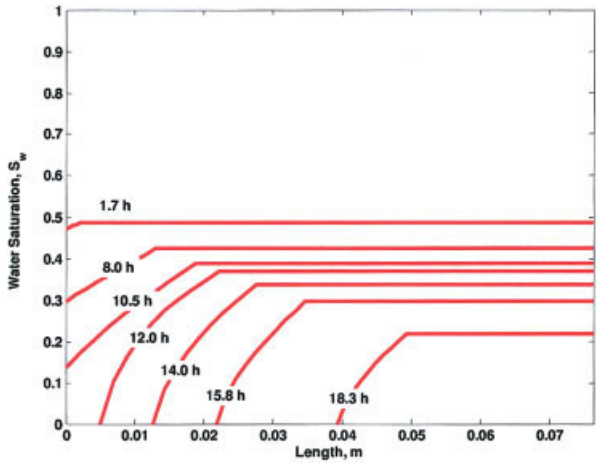

Figure 8. Saturation evolution during injection of a dry gas into a porous medium after the displacement regime has been completed.

Flow parameters from Table 1 (B-15b) for a permeability of 0.085 Darcy and a pressure drop of 0.87 atm. The value of the capillary "wicking" number is 2.8. [Color figure can be viewed in the online issue, which is available at www.interscience.wiley.com]

(a) Films Connected to the Inlet. During this stage, boundary conditions of Eqs. 21 and 40 apply. In the approximation we seek the important variables are: the saturation value $S_r(t_D)$ in the flat portion of the profile downstream, the location $x_r(t_D)$ of the boundary that separates the flat from the variable parts of the profile (Figure 7) and the time at which the films disconnect from the inlet. The quasi-steady approximation near the inlet $(0 < x < x_r)$ gives

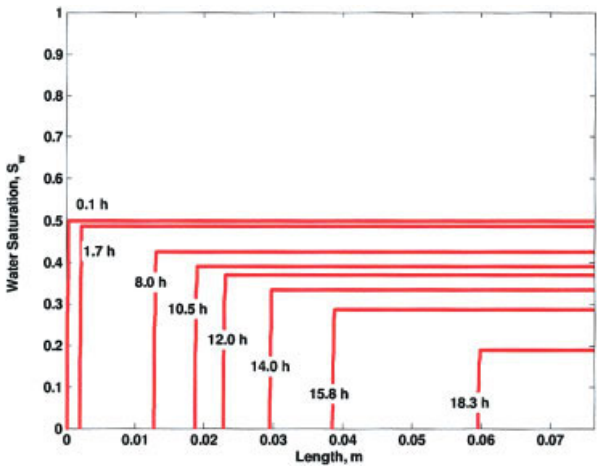

Figure 9. Saturation evolution during injection of a dry gas into a porous medium after the displacement regime has been completed.

Flow parameters from Table 1 (B-15b) for a permeability of 0.085 Darcy and a pressure drop of 0.87 atm. The value of the capillary "wicking" number is 0.005. [Color figure can be viewed in the online issue, which is available at www.interscience.wiley.com]

$$N_{Wi}D(S_w)\frac{dS_w}{dx_D} = u_D(x) = \frac{2\left[1 - C\dfrac{\displaystyle\int_0^{x_D}\frac{d\xi}{k_{rg}(S_w)}}{\displaystyle\int_0^1\frac{d\xi}{k_{rg}(S_w)}}\right]^{-1/2}}{C\left[\displaystyle\int_0^1\frac{d\xi}{k_{rg}(S_w)}\right]} \approx \frac{2}{C\left[\displaystyle\int_0^1\frac{d\xi}{k_{rg}(S_w)}\right]} \quad (41)$$

where the inlet conditions were used for deriving the RHS. This equation can be integrated to give the saturation profile

$$S_w^{3/2} - S_0^{3/2} = \frac{\displaystyle\int_0^{x_D} u_D(x)dx}{N_{Wi}} \approx \frac{2x_D}{CN_{Wi}\left[\displaystyle\int_0^1\frac{d\xi}{k_{rg}(S_w)}\right]} \quad (42)$$

where in the RHS, we approximated the velocity in the integral with its inlet value and defined the inlet saturation $S_o(t_D)$. Its variation with time is obtained implicitly by substituting $x_D = x_r(t_D)$ and $S_w = S_r(t_D)$ in Eq. 42 to obtain one relationship between the three unknowns x_r, S_r, and S_o:

$$S_r^{3/2} - S_0^{3/2} = \frac{2x_r}{CN_{Wi}\left[\displaystyle\int_0^1\frac{d\xi}{k_{rg}(S_w)}\right]} \quad (43)$$

The second relationship is obtained by integrating Eq. 19a in the region of the flat profile ($x_r < x < 1$), to obtain, after some manipulations,

$$(1 - x_r)\frac{dS_r}{dt_D} = -u_D(1) + u_D(x_r) \quad (44)$$

which is similar to Eq. 32. We can use Eq. 19b in the RHS of Eq. 44 to obtain the more explicit expression

$$(1 - x_r)\frac{dS_r}{dt_D} = -\frac{2(1 - C)^{-1/2}}{C\left[\displaystyle\int_0^1\frac{d\xi}{k_{rg}(S_w)}\right]} + \frac{2\left[1 - C\dfrac{\displaystyle\int_0^{x_r}\frac{d\xi}{k_{rg}(S_w)}}{\displaystyle\int_0^1\frac{d\xi}{k_{rg}(S_w)}}\right]^{-1/2}}{C\left[\displaystyle\int_0^1\frac{d\xi}{k_{rg}(S_w)}\right]} \quad (45)$$

However, much can be learned if we take a linearly varying velocity, $du_D/dx = e$ [$\cong k_{rg}^0(1 - C)^{-3/2}$] by simplifying the second term of the RHS of Eq. 19, with constant relative permeability, and corresponding to a constant evaporation rate), in which case Eq. 44 simply gives

$$\frac{dS_r}{dt_D} = -e \quad (46a)$$

or, after integrating,

$$S_r = S_i - et_D \quad (46b)$$

which shows that the flat-profile value decreases linearly in time. The third equation is obtained by integrating Eq. 19a over the whole region (Appendix A),

$$S_r\frac{dx_r}{dt_D} = u_D(x_r) \quad (47a)$$

where in the second term we neglected evaporation arising from gas expansion in the variable saturation region. The evolution of the inlet saturation in terms of the receding saturation is obtained by using Eq. 43:

$$S_0 = \left\{S_r^{3/2} - \frac{2x_r}{CN_{Wi}\left[\displaystyle\int_0^1\frac{d\xi}{k_{rg}(S_w)}\right]}\right\}^{2/3} \quad (47b)$$

The set of the ordinary differential Eqs. 45 and 47a can be solved simultaneously. If we simplify Eq. 47a by neglecting gas expansion throughout the length and integrate, we find the explicit result, after and substituting Eq. 46b,

$$x_r = \frac{1}{e}u_D(0)\ln\left(\frac{S_{wi}}{S_{wi} - et_D}\right) \quad (48)$$

which gives the velocity for the edge of the front. By substituting Eq. 48 into Eq. 47b and rearranging we obtain an expression for the inlet saturation in terms of the dimensionless time:

$$S_0 = \left\{S_r^{3/2} + \frac{1}{e}\ln\left(1 - \frac{et_D}{S_{wi}}\right)\frac{[u_D(0)]^2}{N_{Wi}}\right\}^{2/3} \quad (49a)$$

The time for the disconnection of the films from the inlet end of the sample follows directly:

$$t_D^* = \frac{1 - \exp\left\{-\dfrac{S_r^{3/2}eN_{Wi}}{[u_D(0)]^2}\right\}}{e}S_{wi} \quad (49b)$$

The saturation profile in the region near the inlet is obtained from Eq. 42 based on the knowledge of the inlet saturation S_0 given by Eq. 49a. In the above and the expressions to follow,

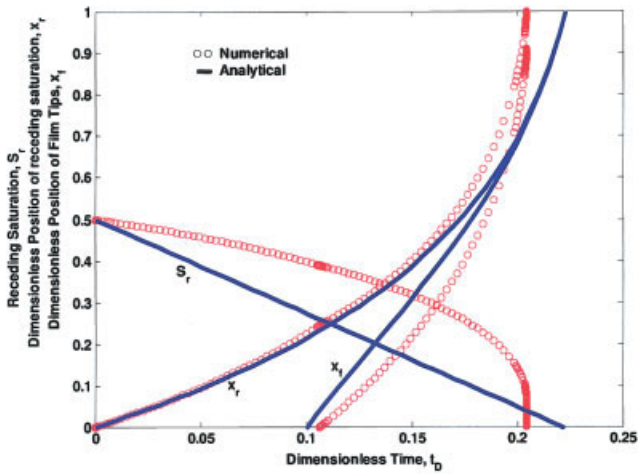

Figure 10. Evolution of the quantities x_r, S_r, and x_f corresponding to dry-gas injection (see Figure 7 for a schematic) for the conditions of Figure 8.

Solid lines denote analytical approximations, circles the numerical results. [Color figure can be viewed in the online issue, which is available at www.interscience.wiley.com]

$u_D(0)$ is approximated to be $2k^0_{rg}/C$, derived from Eq. 19b by assuming constant relative permeability.

(b) Films Disconnected from the Inlet. When the films become disconnected, the drying front moves into the porous medium and a dry region arises, which grows in time (Figure 7). We will denote by x_f the location of the trailing edge of the region, and retain the previous notation for the flat saturation profile. We will proceed as before. Equation 45 remains valid and so does Eq. 41. The latter integrated in the region $x_f < x < x_r$ gives

$$S_w^{3/2} = \frac{\int_{x_f}^{x_D} u_D(x)dx}{N_{Wi}} \approx \frac{2(x_D - x_f)}{CN_{Wi}\left[\int_0^1 \frac{d\xi}{k_{rg}(S_w)}\right]} \tag{50}$$

which evaluated at x_r further becomes

$$S_r^{3/2} = \frac{2(x_r - x_f)}{CN_{Wi}\left[\int_0^1 \frac{d\xi}{k_{rg}(S_w)}\right]} \tag{51}$$

This is the second relation between the three unknowns x_r, S_r, and x_f. The final relation is a version of Eq. 47 obtained upon integration of Eq. 19a over the whole region (Appendix B). We find

$$S_r \frac{dx_r}{dt_D} = u_D(x_r) \tag{52}$$

Again, if we simplify by neglecting gas expansion and integrate, we obtain the explicit result

$$x_r = \frac{1}{e} u_D(0) \ln\left(\frac{S_{wi}}{S_{wi} - et_D}\right) \tag{53}$$

Under the same simplifications, if we assume constant gas flow velocity, we obtain from Eq. 51

$$(x_r - x_f) = \frac{S_r^{3/2} CN_{Wi}}{2}\left[\int_0^1 \frac{d\xi}{k_{rg}(S_w)}\right] \tag{54}$$

which shows that the width of the front is constant for a given receding saturation. When gas expansion is included in the calculations the saturation decreases and thus the width also decreases.

A comparison of the approximate analytical results with the numerical for the evolution in time of the key quantities x_r, S_r, and x_f is shown in Figure 10. The trend shown by the numerical results is similar to that of the prediction of the analytical approximation. The analytical solution, shown in solid line, shows a slower decrease in the receding saturation and consequently slower drying, given the assumption of constant relative permeability.

Comparison with Experiments

The simulations were next compared with experimental results from X-ray imaging.[28] The parameters corresponding to Table 1 were used. Figure 11 shows the results of the comparison with the wet-gas injection case. Overall, the comparison is quite good. The numerical model does not capture the local variations in the experimental saturations (because of the presence of permeability heterogeneity[29]) and causes nonuniform

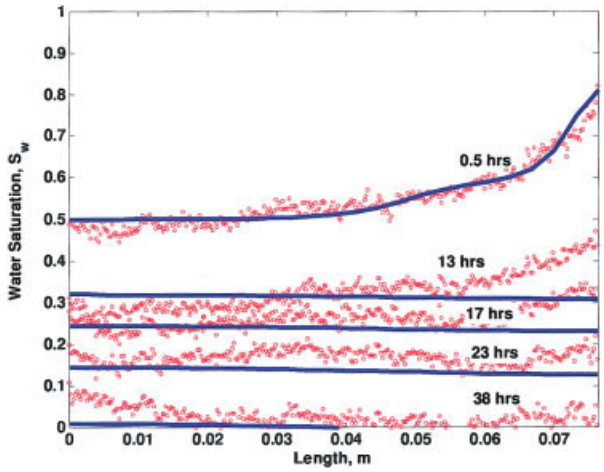

Figure 11. Comparison of water saturation profiles between experimental data obtained from X-ray scanning, shown in empty circles, and the model, shown in solid line for flow-through drying and injection of a wet gas.

Gas flow is from left to right. Flow parameters from Table 1 (B-15b), with the value of the capillary "wicking" number equal to 123. The indicated times are experimental values, whereas the model times are as shown in Figure 1. [Color figure can be viewed in the online issue, which is available at www.interscience.wiley.com]

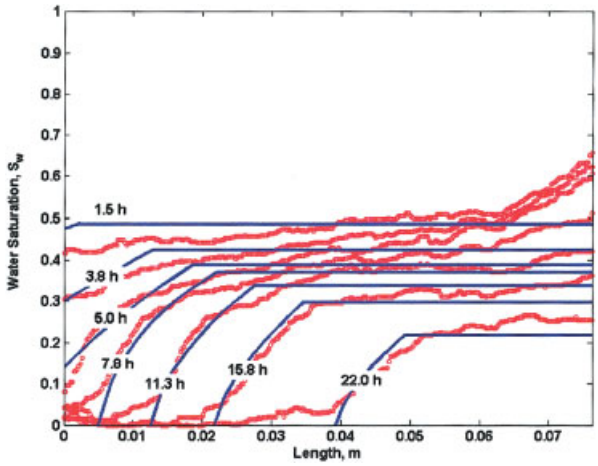

Figure 12. Comparison of water saturation profiles between experimental data obtained from X-ray scanning, shown in empty circles, and the model, shown in solid line for flow-through drying and injection of a dry gas.

Gas flow is from left to right. Flow parameters from Table 1 (B-15b), with the pressure drop equal to 0.87 atm and the value of the capillary "wicking" number equal to 2.8. The experimental times are shown in the plot. Model times are the same as those shown in Figure 8. [Color figure can be viewed in the online issue, which is available at www.interscience.wiley.com]

capillary pressure curves locally. The agreement becomes less satisfactory near the latter stages of the process. Figure 12 shows the corresponding comparison for dry-gas injection. As predicted by the model, two stages develop—when the liquid films are connected and when they become disconnected from the inlet end. The forward moving saturation front is spread as a result of capillary flow, induced by films. The movement of the front is relatively faster toward the later part of the injection process, explained by the fact that the flow rate of gas also increases as more and more of the liquid is removed by both the concentration difference at the inlet and by the compressibility effect. The model predicts the essential features of the spreading drying front and the receding saturations resulting from the compressibility of gas. The experimental front, however, shows saturations that taper off more gradually than in the model. We suspect that this arises from thin film flow effects that exist in the experiments but are less well captured in the model.

The experimental data for dry-gas injection indicate a slightly slower rate of drying than predicted in the model. This can be explained by the fact that saturation profiles at the end of displacement were taken as uniform in the model, whereas in the experiments significant capillary end effects exist. The latter can cause a reduction in the gas flow rates and thus lesser evaporation at the drying front.

Conclusions

In this article, we modeled flow-through drying in porous media under completely water saturated and dry-gas injection conditions. The first case finds application in the flow of a gas condensate, where as a result of the pressure drop liquid condenses, thus hindering the gas flow. Flow-through drying aims at removing the so-developed blocks. Gas compressibility is the main mechanism that drives drying under such saturated conditions. The model includes capillarity, which facilitates the redistribution of liquid through capillary flow and improves the drying rates, arising from the transport of liquid from low drying-rate areas in the upstream end to higher drying-rate areas. In the case of dry-gas injection, a drying front develops, when the liquid loses connectivity to the inlet end. The front has a width that depends on the capillary "wicking" number of the displacement. However, because of the gas expansion, the downstream saturation of the front is not constant, as in typical fractional flow problems, where shocks form, but decreases with time as the front propagates. In addition to numerical results, we have developed analytical approximations that were shown to compare reasonably well with the numerical predictions. The results were also found in good overall agreement with experimental results for two typical cases representing wet-gas and dry-gas injections in Berea sandstone. The gas flow rate also is affected by the rate of evaporation, which is in-turn coupled to the gas flow itself. It is shown that for a higher capillary number the gas flow rate recovery is also higher as a result of the greater evaporation rates.

Notation

a_g = dimensionless geometric factor
a_{gm} = modified dimensionless geometric factor
C = dimensionless pressure drop
D = Darcy, unit of permeability, 9.8×10^{-13} m^2
e = dimensionless constant $[=k^0_{rg}(1 - C)^{-3/2}]$
f' = dimensionless fractional flow rate
f = dimensionless fractional mobility
g = gravitational constant, 9.8 m/s^2
i = number of corner films in a pore
k = gas permeability at mean pressure, $D(9.87 \times 10^{-13}$ m$^2)$
k_{rg} = relative permeability to gas
k^0_{rg} = endpoint relative permeability to gas
k_{rj} = relative permeability of phase j
k^0_{rj} = endpoint relative permeability of phase j
L = length of core, m
N_{Wi} = dimensionless wicking number
P = pressure, atm
P_c = capillary pressure, atm
P_s = saturation pressure, atm
q = volumetric flux by Darcy's law, m/s
q_x = volumetric flux of liquid in a single corner, m/s
Q_x = volumetric flow rate of liquid in a single corner
r = radius of curvature of liquid film in a corner, m
r_c = hydraulic radius of a rectangular capillary, m
R_g = universal gas constant, 8.314 J mol^{-1} K^{-1}
S = saturation
S_{ir} = residual saturation of phase j
S = normalized saturation
T = temperature, °C
u = velocity, m^3/s
y_w = mole fraction of water in gas
z = gas compressibility factor

Subscripts

0 = inlet position of sample
L = outlet position of sample
g = gas phase
w = water phase
D = dimensionless quantity
f = pertains to film region
T = total value

Greek letters

α = concentration of water in gas phase, mol/m^3
β = concentration of water in liquid phase, mol/m^3
γ = interfacial tension, N/m; interfacial tension of air–water interface, kg/s^2
ε = drying time-scaling factor
ϕ = porosity of core
λ = gas mobility at mean pressure
λ_r = relative gas mobility
μ = viscosity, kg m^{-1} s^{-2}
π = scaled pressure, atm
Π = modified pressure, $P_g - P_s$ atm
ρ = density, kg/m^3
τ = scaled time ($=\varepsilon t$), s

Literature Cited

1. Whitaker D. Simultaneous heat, mass and momentum transfer in porous media: A theory of drying. *Adv Heat Transfer*. 1977;1:119-203.
2. Prat M. Isothermal drying of non-hygroscopic capillary-porous materials as an invasion percolation process. *Int J Multiphase Flow*. 1995; 21:875-892.
3. Figus C, Le Bray Y, Bories S, Prat M. Heat and mass transfer with phase change in a porous structure partially heated: Continuum model and pore network simulations. *Int J Heat Mass Transfer*. 1999;42: 2557-2569.
4. Prat M, Bouleux F. Drying of capillary porous media with a stabilized front in two dimensions. *Phys Rev E*. 1999;60:5647-5656.
5. Prat M. Recent advances in pore-scale models for drying of porous media. *Chem Eng J*. 2002;86:153-164.
6. Plourde F, Prat M. Pore network simulations of drying of capillary porous media: Influence of thermal gradients. *Int J Heat Mass Transfer*. 2003;46:1293-1307.
7. Luikov AV. *Heat and Mass Transfer in Capillary Porous Media*. London, UK: Pergamon Press; 1966.
8. Allerton J, Brownell LE, Katz DL. Through-drying of porous media. *Chem Eng Prog*. 1949;45:619-635.
9. Mahadevan J, Sharma MM. Clean up of water blocks in low permeability formations. *Soc Pet Eng J*. 2005;10(3):238–246.
10. Kamath J, Laroche C. Laboratory-based evaluation of gas well deliverability loss caused by water blocking. *Soc Pet Eng J*. 2003;Mar.:71-80.
11. Zuluaga E, Lake LW. Modeling of experiments on water vaporization for gas injection. Proceedings of the 2004 SPE Eastern Regional Meeting, Sep. 15–17, Charleston, WV; 2004.
12. Woods AW, Fitzgerald SD. The vaporization of a liquid front moving through a hot porous rock: Part 2. Slow injection. *J Fluid Mech*. 1997;343:303-316.
13. Whitaker S. Toward a diffusion theory of drying. *Ind Eng Chem Fundam*. 1977;16:408-414.
14. Lenormand R, Zarcone C. Role of roughness and edges during imbibition in square capillaries. *Soc Pet Eng J*. 1984;13264.
15. Lenormand R. Liquids in porous media. *J Phys Condens Matter*. 1992;2:SA79.
16. Dullien AL, Zarcone C, MacDonald IF, Collins A, Bochard DE. The effects of surface roughness on the capillary pressure curves and the heights of capillary rise in glass bead packs. *J Colloid Interface Sci*. 1997;127:36.
17. Shaw TM. Drying as an immiscible displacement process with fluid counterflow. *Phys Rev Lett*. 1987;59:1671-1675.
18. Laurindo JB, Prat M. Modeling of drying in capillary porous media: A discrete approach. *Drying Technol*. 1998;16:1769.
19. Yiotis AG, Boudouvis AG, Stubos AK, Tsimpanogiannis IN, Yortsos YC. The effect of liquid films on the drying of porous media. *AIChE J*. 2004;50:2721-2737.
20. Lake LW. *Enhanced Oil Recovery*. Englewood Cliffs, NJ: Prentice Hall; 1989.
21. Corey AT. *Mechanics of Heterogeneous Fluids in Porous Media*. Fort Collins, CO: Water Resources Publications; 1977.
22. van Genuchten MTh. A closed-form equation for predicting the hydraulic conductivity of unsaturated soils. *Soil Sci Soc Am J*. 1980;44: 892-898.
23. Wilkinson D. Percolation effects in immiscible displacement. *Phys Rev A*. 1986;34:1380-1391.
24. Ransohoff TC, Radke CJ. Laminar flow of a wetting liquid along the corners of a predominantly gas-occupied non-circular pore. *J Colloid Interface Sci*. 1988;121;392.
25. Dong M, Chatzis I. The imbibition and flow of a wetting liquid along the corners of a square capillary tube. *J Colloid Interface Sci*. 1995; 172:278.
26. Toledo PG, Davis TH, Scriven LE. Capillary hyperdispersion of wetting liquids in fractal porous media. *Transport Porous Media*. 1993;10:81-94.
27. Mahadevan J, Sharma MM, Yortsos YC. Evaporative clean-up of water-block in gas wells. SPE 94215. Proceedings of the Society of Petroleum Engineers Production and Operations Symposium, Apr. 17–19, Oklahoma City, OK; 2005.
28. Mahadevan J, Sharma MM, Yortsos YC. Water removal from porous media by gas injection: Experiments and simulation. *Transport Porous Media*. 2006; in press.
29. Chang J, Yortsos YC. Effect of capillary heterogeneity on Buckley–Leverett displacement. *Soc Pet Eng Reservoir Eng*. 1992;7:285-293.
30. Mahadevan J. *Flow Through Drying of Porous Media*. PhD Dissertation. Austin, TX: The University of Texas; August 2005.

Appendix A

By integrating Eq. 19a over the region ($0 < x < 1$), and applying the boundary conditions for dry gas injection, we find

$$\frac{d}{dt_D}\int_0^1 S_w dx = -u_D(1) \tag{A1}$$

We decompose

$$\int_0^1 S_w dx = \int_0^{x_r} S_w dx + (1 - x_r)S_r \tag{A2}$$

and evaluate the first integral

$$\int_0^{x_r} S_w dx = N_{Wi}\int_{S_0}^{S_r} \frac{SD(S)}{u_D(x_D)}\, dS \tag{A3}$$

Taking the time derivatives and substituting in Eq. A2 we obtain

$$\int_{S_0}^{S_r} \frac{\partial}{\partial t_D}\left[\frac{SD(S)}{u_D(x_D)}\right] dS + N_{Wi}\left[\frac{S_r D(S_r)}{u_D(x_r)}\right]\frac{dS_r}{dt_D} - N_{Wi}\left[\frac{S_0 D(S_0)}{u_D(0)}\right]\frac{dS_0}{dt_D} - S_r\frac{dx_r}{dt_D} = -u_D(x_r) \tag{A4}$$

where we made use of Eq. 44. With the assumption of quasi-steady state in the inlet region, Eq. A4 becomes

$$S_r\frac{dx_r}{dt_D} = u_D(x_r) \tag{A5}$$

which leads to Eq. 47 in the text.

Appendix B

By integrating Eq. 19a over the region ($x_f < x < 1$) and using the boundary condition

$$N_{Wi}D(S_w)\left.\frac{\partial S_w}{\partial x_D}\right|_{x_f} = u_D(x_f) \tag{B1}$$

we find

$$\frac{d}{dt_D}\int_{x_f}^{1} S_w dx = -u_D(1) \tag{B2}$$

We decompose, as before,

$$\int_{x_f}^{1} S_w dx = \int_{x_f}^{x_r} S_w dx + (1 - x_r)S_r \tag{B3}$$

and evaluate the first integral

$$\int_{x_f}^{x_r} S_w dx = N_{Wi}\int_{0}^{S_r} \frac{SD(S)}{u_D(x_D)}\, dS \tag{B4}$$

Taking the time derivatives and substituting in Eq. B2 we obtain

$$N_{Wi}\int_{0}^{S_r} \frac{\partial}{\partial t_D}\left[\frac{SD(S)}{u_D(x_D)}\right] dS + N_{Wi}\left[\frac{S_r D(S_r)}{u_D(x_r)}\right]\frac{dS_r}{dt_D} - S_r\frac{dx_r}{dt_D} = -u_D(x_r) \tag{B5}$$

where we made use of Eq. 44. With the quasi-steady state assumption, Eq. B5 becomes

$$S_r\frac{dx_r}{dt_D} = u_D(x_r) \tag{B6}$$

Manuscript received Oct. 20, 2005, and revision received Mar. 7, 2006.